American Mineralogist, Volume 110, pages 908–918, 2025

Influence of cation disorder on the mineral physics of ankerite

Azzurra Zucchini[1,*], Tiziana Boffa Ballaran[2], Maximiliano Fastelli[1], Davide Comboni[3,†], Michael Hanfland[4], Francesco Frondini[1], and Paola Comodi[1]

[1]Department of Physics and Geology, University of Perugia, Piazza Università, 06100 Perugia, Italy
[2]Bayerisches Geoinstitut, University of Bayreuth, D-95440 Bayreuth, Germany
[3]Department of Earth Sciences "Ardito Desio", University of Milan, Via Mangiagalli 34, 20133 Milano, Italy
[4]European Synchrotron Radiation Facility, 71 avenue des Martyrs, 38000 Grenoble, France

Abstract

The structural evolution and compressibility of ordered and disordered ankerite were investigated at pressures up to ~25 GPa using synchrotron single-crystal X-ray diffraction in a diamond-anvil cell. Ordered ankerite (space group $R\bar{3}$) undergoes a discontinuous phase transition between 12.15 and 13.45 GPa to a high-pressure structure called ankerite-II (space group $P\bar{1}$) that has Ca in an eightfold coordination. Disordered ankerite ($R\bar{3}c$ space group) does not undergo a phase transition in the investigated pressure range.

A Birch-Murnaghan equation of state was used to fit the volume compressibility. Ordered ankerite [K_{0V} = 95(1) GPa, K' = 3.8(3)] appears slightly more compressible than disordered ankerite [K_{0V} = 99(1) GPa, K' = 2.7(1)]. The phase transition in ordered ankerite has a change in volume of ~0.6% and $K_{13.45V}$ = 110(11) GPa, K' = 7(3) for ankerite-II. The possible significance of this different behavior of ordered and disordered ankerite is discussed.

Keywords: Ankerite, high pressure, synchrotron, single-crystal X-ray diffraction, compressibility

Introduction

Carbonates are key phases in the Earth's carbon cycle (Litasov et al. 2020). They have stability fields that extend from ambient conditions (shallow C cycle) to low-pressure hydrothermal systems to high-pressure–high-temperature (HP–HT) conditions typical of the upper mantle, lower mantle, and transition zone (e.g., Biellmann and Gillet 1992; Luth 2001; Zhu and Ogasawara 2002; Buob et al. 2006; Hammouda et al. 2011; Zucchini et al. 2014, 2017; Cerantola et al. 2017; Binck et al. 2020).

The most abundant carbonates in nature are calcite ($CaCO_3$, space group $R\bar{3}c$), magnesite ($MgCO_3$, space group $R\bar{3}c$), and dolomite [$CaMg(CO_3)_2$, space group $R\bar{3}$]. The addition of small transition metals to dolomite does not change its space group. Moreover, the Mg^{2+}-Fe^{2+} substitution is a complete solid solution in the $FeCO_3$-$MgCO_3$ systems, whereas in the $FeCO_3$-$MgCO_3$-$CaCO_3$ system, the substitution is limited to ankerite having the chemical formula $Ca(Mg_{1-x}Fe_x)(CO_3)_2$, where $0 \leq x \leq 0.7$, and being isostructural with dolomite.

In naturally $R\bar{3}$ occurring carbonates, there is an ordered alternation of cations between structural layers. At HT, cations start to randomly distribute among the different cationic sites, giving rise to disordered structures (Reeder and Wenk 1983; Zucchini et al. 2012a, 2012b). The critical temperature (T_C) for the order-disorder transition, at which the disordering process is complete and the space group changes from $R\bar{3}$ (dolomite-like structure) to $R\bar{3}c$ (calcite-like structure), is strongly influenced by the cationic species. In fact, a T_C of ~1200 °C was attributed to dolomite (Zucchini et al. 2012a, 2012b; Hammouda et al. 2011), and it decreases with increasing Fe content (Franzolin et al. 2012).

High-pressure behavior of carbonates

Structural parameters such as chemical composition and cation order/disorder strongly influence a carbonate's stability under non-ambient conditions, and considerable efforts have been made to constrain the phase stability of carbonates. Given the similarity of ankerite and dolomite, the known phase transitions in the system $CaCO_3$-$MgCO_3$ are given in Table 1. The mineral physics of dolomite at HP is strongly influenced by its crystal-chemical features. Experimental and theoretical studies on the HP phase transitions of dolomite as a function of disorder (Zucchini et al. 2014, 2017) showed that disordered dolomite does not transform to the HP polymorph dolomite-II, at least up to ~30 GPa. Moreover, the Mg substitution by Fe has important effects on the HP behavior of the mineral, in terms of compressibility, structural stability, and thermoelastic properties (Zhang et al. 1998; Merlini et al. 2016), i.e., the transition pressures were shown to slightly decrease (~2–4 GPa lower) with increasing Fe content in dolomite (Merlini et al. 2012, 2017; Zhao et al. 2020). However, although the effect of Fe on the behavior of ordered dolomites has been investigated (e.g., Ross and Reeder 1992; Merlini et al. 2016; Chuliá-Jordán et al. 2021), the effect of cation disorder on the compressibility and possible phase transitions occurring in ankerite is unknown, in spite of its importance, since at mantle conditions carbonates are expected to be disordered (Zucchini et al. 2012a, 2012b; Franzolin et al. 2012). For these reasons, in this study, synchrotron single-crystal X-ray diffraction (SC-XRD) experiments have been performed to constrain the HP behavior of ordered and disordered ankerite and to give insight into the influence of cation disorder on its structural evolution.

* Corresponding author E-mail: azzurra.zucchini@unipg.it Orcid https://orcid.org/0000-0002-5603-8353
† Orcid https://orcid.org/0000-0001-6445-3736

0003-004X/25/0006–908$05.00/DOI: https://doi.org/10.2138/am-2024-9495

Table 1. Known HP polymorphs in selected carbonates

Mineral/formula	*P* (GPa)	*T* (K)	Polymorph	Space group
$CaCO_3$	1.5	RT	$CaCO_3$-II	$P2_1/c$[a,b,c]
	2.0	RT	$CaCO_3$-III	$P\bar{1}$[d]
	3.0	RT	$CaCO_3$-IIIb	$P\bar{1}$[d]
	~2	~150	aragonite	$Pmcn$[e]
	15	RT	$CaCO_3$-VI	$P\bar{1}$[f]
	~30	RT	$CaCO_3$-VII	$P2_1/c$[g]
	~42	1400	postaragonite	$Pmmm$[h]
$MgCO_3$	80	2100–2200	$MgCO_3$-II	$C2/m$[i,l]
	138	3000	$MgCO_3$-III	$P2_12_12_1$[i,l]
$MgCa(CO_3)_2$	14–18	RT	dolomite-II	$P\bar{1}$[m,n,o,p]
	~35	RT	dolomite-III	$P\bar{1}$[f]
	~36	RT	dolomite-IIIb	R3[n]
	~41	RT	dolomite-IIIc	R3[n]
	~115	Stabilized at 2500	dolomite-IV	$Pnma$[n]

Notes: *P* and *T* refer to minimum transition pressure and temperature conditions, respectively. RT means room temperature.
[a] Merrill and Basset (1975).
[b] Hatch and Merrill (1981).
[c] Harris et al. (1998).
[d] Pippinger et al. (2015).
[e] Zhao et al. (2022).
[f] Merlini et al. (2012).
[g] Gavryushkin et al. (2017).
[h] Li et al. (2018).
[i] Oganov et al. (2008).
[l] Li et al. (2020).
[m] Zucchini et al. (2014).
[n] Merlini et al. (2017).
[o] Efthimiopoulos et al. (2017).
[p] Vennari and Williams (2018).

Materials and Methods

Starting materials

Two different samples were used in this work. One (hereafter referred to as ank-ord, Fig. 1a) is a natural ankerite with chemical formula $Ca_{1.0(2)}[Mg_{0.28(5)}Fe_{0.7(1)}Mn_{0.04(1)}](CO_3)_2$ kindly provided by the Natural History Museum of Copenhagen (Denmark). The other (hereafter referred to as ank-dis, Fig. 1c) is a fully disordered ankerite, obtained by annealing the ank-ord sample at 750 °C and 3 GPa for 4 h. Thermal treatments were carried out using a 1/2″ diameter internally heated piston-cylinder apparatus located at the Bayerisches Geoinstitut (Bayreuth, Germany) following the procedure described for dolomite disordering in Zucchini et al. (2012a).

Single-crystal synchrotron X-ray diffraction

Experiments were carried out at the ID-15B beamline at European Synchrotron Radiation Facility, Grenoble, France. Intensities were collected on a large-area EIGER2 X 9M CdTe (340 × 370 mm) hybrid pixel detector. The X-ray wavelength was monochromated to 0.410374 Å. A membrane-type diamond-anvil cell (DAC) with an opening angle of 64° and 600 μm culet diamonds was used. Helium was the pressure-transmitting medium (Klotz et al. 2009) and ruby the pressure calibrant (Mao et al. 1986), loaded into the DAC together with two single crystals, ank-ord (~35 × 22 × 30 μm) and ank-dis (~35 × 35 × 30 μm). The pre-indented stainless-steel gasket had a 300 μm diameter hole. The sample-to-detector distance was 181.0480 mm, which was calibrated, along with the wavelength, using Si standard and Fit2D software (Hammersley et al. 1996). Operating conditions for HP data collections were 64° ω-rotation, 0.5° step size, and 0.3 s step time. Data at ambient pressure were collected with the crystal in DAC, and then HP data were obtained up to ~25 GPa. The attempt to collect data during decompression was made. However, the quality of the data for the highest pressure at 24.98 GPa for ank-ord and the data during decompression for both ank-ord and ank-dis was not high enough for single-crystal structural analysis. The only data good enough for unit-cell determination and structure refinement, under decompression, were those of the recovered crystals at room pressure.

Pressure was measured before and after each data collection, and gasket relaxation was ensured by waiting ~15 min after changing the load. The typical time taken for a complete data collection at each pressure was within 3 min.

Collected data were integrated by means of the CrysAlisPro software (Rigaku Oxford Diffraction, 2020, 1.171.42.49, Agilent Technologies, U.K.), and the empirical absorption correction was applied as implemented in SCALE3 ABSPACK scaling algorithm. Structure refinements were carried out using ShelXle program (Hübschle et al. 2011). Neutral atomic scattering factors were used.

Because of the limited number of reflections in DAC data collection, we could not base our crystal structure refinements on systematic absences to test whether the ank-dis space group was $R\bar{3}$ (partial disorder) or $R\bar{3}c$ (full disorder). Thus, both ank-ord (Fig. 1a) and ank-dis were initially refined in $R\bar{3}$ space group. Cation site occupancy was refined at (0, 0, 0) and (0, 0, 1/2) atomic positions, checking for Ca/Mg/Fe disordering occurrence. The total occupancy factor per site was fixed to 1 and, at first, no chemical constraints were used. The refined Ca/Mg/Fe total content agreed with the chemical analysis of the analyzed samples; thus, structure refinements were finalized applying constraints for chemical composition. In ank-dis, site-scattering values for the two sites are consistent with Ca/Mg/Fe being distributed statistically at both (0, 0, 0) and (0, 0, 1/2) sites, i.e., fully disordered. In fact, the refined numbers of electrons at (0, 0, 0) and (0, 0, 1/2) are 20.8(6) and 21.0(6), respectively. Moreover, z_C, y_O, and z_O atomic coordinates, which lie in general positions in the ordered dolomite, approached a special position in the disordered ankerite. Thus, ank-dis was refined in the $R\bar{3}c$ space group (Fig. 1c).

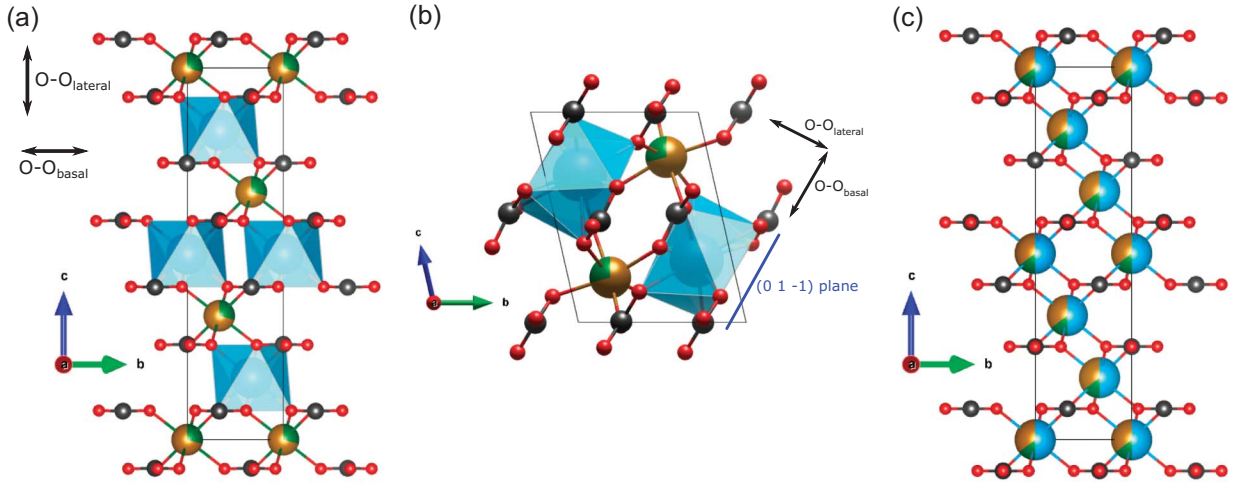

Figure 1. Crystal structure of (**a**) ank-ord at 0.47 GPa, (**b**) ank-ord-II at 21.97 GPa, and (**c**) ank-dis at 0.47 GPa, down the **a** axis. The graphical explanation of d(O-O)$_{lateral}$ and d(O-O)$_{basal}$, as well as the projection of the $(01\bar{1})$ lattice plane in ank-ord-II, is also shown. For ank-dis, d(O-O)$_{lateral}$ and d(O-O)$_{basal}$ are the same as in ank-ord. Colors: blue is Ca, light brown is Fe, green is Mg, gray is C, and red is O. (Color online.)

The distortion of the coordination polyhedra was analyzed with the program Ivton (Balić Žunić and Makovicky 1996). The compressibility of the analyzed samples was calculated from the measured unit-cell parameters using a Birch-Murnaghan Equation of State (EoS) as implemented in the EosFit GUI (Gonzalez-Platas et al. 2016).

Results

The good crystallinity of the samples was maintained in the analyzed pressure (P) range. Details of data collections and refinements are deposited (Online Materials[1] Table S1) together with the crystallographic information files (Online Materials[1] CIFs). Data for ank-ord were analyzed in space group $R\bar{3}$ up to 12.15 GPa. As noted above, refinement of cation site occupancies showed that ank-ord has full cation ordering, i.e., Ca and (Mg,Fe) are on separate sites (Fig. 1a). Above 13 GPa, rhombohedral symmetry is broken and data could be indexed only with a triclinic unit cell indicating a phase transition from ankerite to a high-pressure polymorph, here referred to as ankerite-II ("ank-ord-II"), because of its similarity with the structure of dolomite-II (Merlini et al. 2012). Structure refinements of ank-ord-II were performed in space group $P\bar{1}$ (Fig. 1b). In contrast to the phase transition observed for ank-ord, no transition was observed for ank-dis in the same P range, with structure refinements indicating space group $R\bar{3}c$. The data collected at room P after decompression showed that, while the disordered sample maintains the $R\bar{3}c$ structure, the ordered sample recovers the $R\bar{3}$ structure typical of ank-ord. Thus, the reversibility of the ank-ord to ank-ord-II phase transition is confirmed.

Equation of state and compressibility of ankerite

Unit-cell parameters and volumes for ank-ord, ank-ord-II, and ank-dis are shown in Figure 2 and Table 2. The evolution of the unit-cell volume with P (Fig. 2a) shows a significant change at the ank-ord → ank-ord-II transition between 12.15 and 13.45 GPa. The unit-cell parameters decrease as P increases in all three crystal structures, and the c parameter always shows the highest compressibility. The **a** axis is the least compressible axis and it even expands with increasing P in the ank-ord II structure (Fig. 2).

Data were fitted using the third order Birch Murnaghan (BM) Equation of State (EoS) (Birch 1952) as suggested by the "normalized pressure" (F) – "Eulerian finite strain" (f) plots (Online Materials[1] Fig. S1). Results of fitting are given in Table 3 where data for ank-ord-II are given using as reference pressure, instead of the room conditions, the first measured pressure point after the phase transition, that is 13.45 GPa. As the BM fitting could not

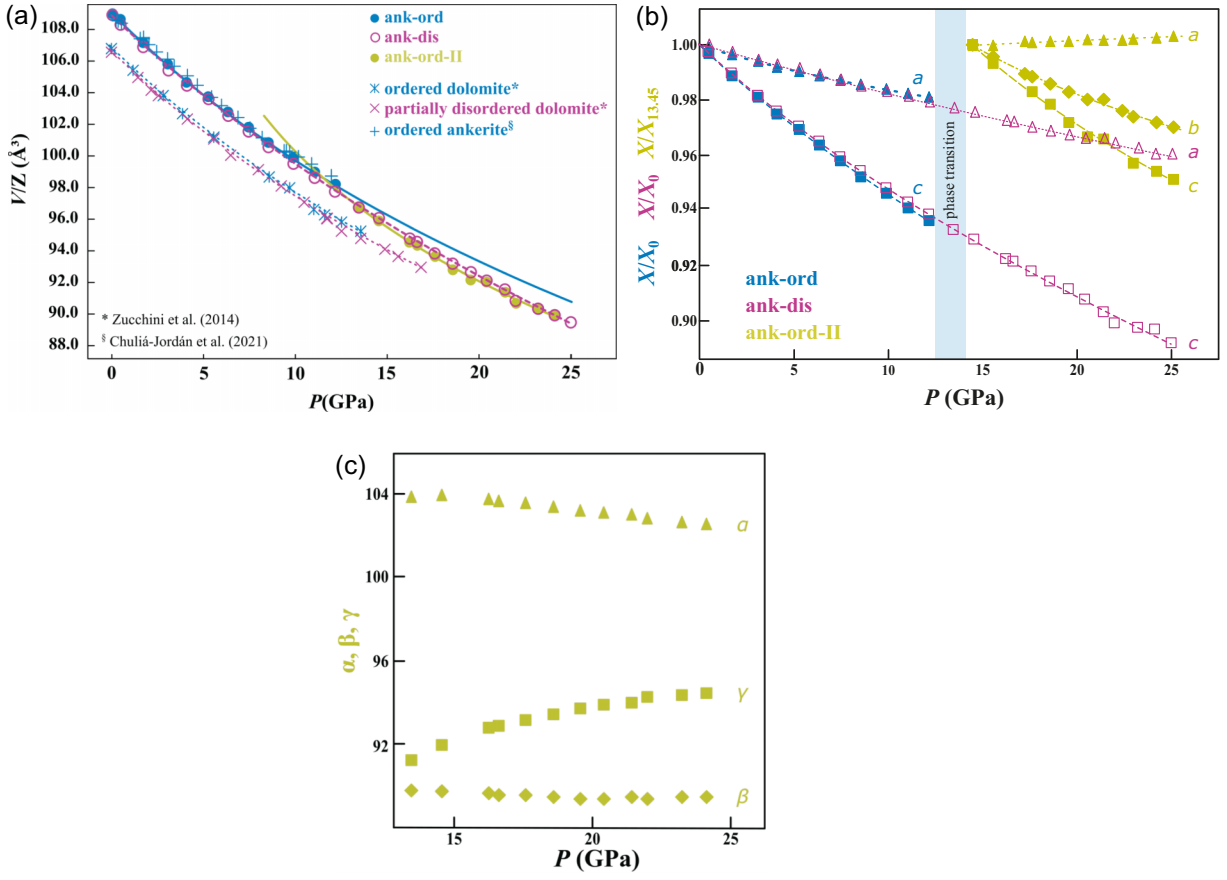

Figure 2. Pressure dependence of (**a**) volume per formula unit (V/Z), (**b**) cell parameters of ank-ord (blue) and ank-dis (purple) normalized with respect to their room-pressure values and that of ank-ord-II (green) normalized with respect to the values at 13.45 GPa, (**c**) angles in ank-ord-II. Curves are the third-order Birch Murnaghan EoS with the only exception of the a parameter of ank-ord-II where the line represents a linear compressibility (see text for details). (Color online.)

Table 2. Unit-cell parameters (Å) listed together with the used pressures (GPa) for ank-ord ($R\bar{3}$, $Z = 3$), ank-ord-II ($P\bar{1}$, $Z = 2$), ank-dis ($R\bar{3}c$, $Z = 3$)

P	*a*	*b*	*C*	α	β	γ	*V*	*P*	*a*	*c*	*V*
ank-ord								**ank-dis**			
0.00	4.8327(2)		16.171(1)				327.07(1)	0.00	4.8279(2)	16.1916(9)	326.83(3)
0.00[a]	4.8314(2)		16.1750(13)				326.98(1)	0.00[a]	4.82714(14)	16.1925(9)	326.76(3)
0.47	4.8293(2)		16.1328(9)				325.84(3)	0.47	4.8216(2)	16.1487(8)	325.13(2)
1.71	4.8166(2)		16.0010(9)				321.48(3)	1.71	4.80899(2)	16.0236(9)	320.92(2)
3.09	4.8049(2)		15.8738(9)				317.38(3)	3.09	4.79521(2)	15.893(8)	316.48(2)
4.09	4.7942(2)		15.7725(10)				313.95(3)	4.09	4.7872(2)	15.8009(11)	313.59(3)
5.27	4.7867(2)		15.6809(11)				311.15(4)	5.27	4.7808(3)	15.7132(13)	311.03(5)
6.34	4.7789(2)		15.5882(10)				308.31(4)	6.34	4.7698(1)	15.6252(9)	307.86(3)
7.45	4.7710(2)		15.4944(11)				305.44(4)	7.45	4.7609(2)	15.5314(11)	304.88(3)
8.53	4.7634(2)		15.3982(10)				302.58(4)	8.53	4.7498(5)	15.453(3)	301.92(7)
9.89	4.7552(2)		15.3003(13)				299.62(5)	9.89	4.7406(2)	15.3517(11)	298.78(3)
11.04	4.7472(2)		15.2128(13)				296.90(5)	11.04	4.7321(3)	15.2688(13)	296.1(3)
12.15	4.7410(2)		15.1366(17)				294.64(6)	12.15	4.7221(2)	15.1986(9)	293.5(3)
ank-ord-II								13.45	4.7117(2)	15.1084(11)	290.47(3)
13.45	4.743(2)	5.686(2)	7.393(3)	103.97(3)	89.73(3)	91.22(3)	193.4(1)	14.54	4.7042(4)	15.052(2)	288.46(4)
14.54	4.7578(9)	5.6609(9)	7.342(2)	104.00(2)	89.82(2)	92.00(1)	191.74(7)	16.22	4.6902(3)	14.9383(16)	284.59(4)
16.22	4.765(1)	5.6251(9)	7.272(2)	103.78(2)	89.73(2)	92.83(2)	189.08(8)	16.61	4.6875(3)	14.9231(16)	283.96(4)
16.61	4.763(1)	5.619(1)	7.265(2)	103.75(2)	89.68(2)	92.94(2)	188.63(8)	17.57	4.6782(4)	14.866(2)	281.77(5)
17.57	4.765(2)	5.604(1)	7.231(3)	103.63(3)	89.65(3)	93.25(2)	187.3(1)	18.55	4.6714(5)	14.807(3)	279.82(7)
18.55	4.765(2)	5.587(2)	7.181(3)	103.41(3)	89.53(3)	93.55(2)	185.61(9)	19.54	4.6647(8)	14.762(5)	278.19(11)
19.54	4.768(2)	5.571(1)	7.142(3)	103.22(3)	89.46(3)	93.80(3)	184.3(1)	20.40	4.661(8)	14.701(5)	276.59(12)
20.40	4.76(1)	5.571(1)	7.136(2)	103.19(2)	89.48(3)	93.95(2)	184.1(1)	21.39	4.6587(7)	14.627(5)	274.93(11)
21.39	4.767(1)	5.549(1)	7.110(2)	103.08(2)	89.52(2)	94.05(2)	182.74(8)	21.97	4.6506(4)	14.5619(19)	272.75(5)
21.97	4.769(1)	5.535(1)	7.070(2)	102.86(2)	89.50(2)	94.33(2)	181.41(9)	23.20	4.6419(2)	14.5359(15)	271.25(3)
23.20	4.771(1)	5.523(1)	7.048(2)	102.74(2)	89.53(2)	94.43(2)	180.58(7)	24.10	4.6329(7)	14.526(6)	270.02(12)
24.10	4.774(1)	5.513(2)	7.026(3)	102.61(3)	89.52(3)	94.54(2)	179.9(1)	24.98	4.6317(5)	14.462(3)	268.68(8)

Note: *P* uncertainty is 0.05 GPa.
[a] Data under decompression.

be used to calculate the expansion of the *a* parameter with increasing *P*, we calculated a linear compressibility, to show that this parameter has a very small negative compressibility. Results of linear fitting gave $\beta_a = -0.0007(1)$ GPa^{-1} (Fig. 2b).

Table 3. EoS parameters obtained from the compressibility analysis of the three analyzed crystal structures

	ank-ord	ank-dis		ank-ord-II
EoS				
BM3				
V_0	327.1 (2)	326.6 (2)	$V_{13.45}$	193.5 (2)
K_{0V}	95 (1)	99 (1)	$K_{13.45V}$	110 (11)
K'_V	3.8 (3)	2.7 (1)	K'_V	7 (3)
a_0	4.83265 (3)	4.8263 (9)	$b_{13.45}$	5.683 (5)
M_{0a}	471 (13)	507 (11)	$M_{13.45b}$	258 (33)
M'_a	33 (4)	8.4 (9)	M'_b	20 (8)
c_0	16.171 (1)	16.19 (1)	$c_{134.5}$	7.392 (9)
M_{0c}	155 (2)	155 (3)	$M_{13.45c}$	161 (17)
M'_c	6.1 (3)	7.4 (2)	M'_c	10 (3)
Polyhedra				
M1			**M1**	
V_0	17.73 (2)	15.09 (1)	$V_{14.54}$	22.6 (2)
K_{0M1}	81 (1)	79.7 (7)	$K_{14.54M1}$	81 (10)
d(O-O)$_{\text{lateral(0)}}$	3.431 (2)	3.250 (2)	d(O-O)$_{\text{lateral(14.54)}}$	3.13 (2)
$M_{0d\text{(O-O)lateral}}$	144 (3)	157 (3)	$M_{14.54d\text{(O-O)lateral}}$	91 (12)
d(O-O)$_{\text{basal(0)}}$	3.277 (2)	3.109 (3)	d(O-O)$_{\text{basal(14.54)}}$	3.172 (4)
$M_{0d\text{(O-O)basal}}$	500 (25)	395 (13)	$M_{14.54d\text{(O-O)basal}}$	411 (42)
M2			**M2**	
V_0	12.86 (2)		$V_{14.54}$	11.32 (9)
K_{0M2}	91 (2)		$K_{14.54M2}$	186 (52)
d(O-O)$_{\text{lateral(0)}}$	3.059 (1)		d(O-O)$_{\text{lateral(14.54)}}$	2.93 (2)
$M_{0d\text{(O-O)lateral}}$	203 (5)		$M_{14.54d\text{(O-O)lateral}}$	307 (127)
d(O-O)$_{\text{basal(0)}}$	2.965 (1)		d(O-O)$_{\text{basal(14.54)}}$	2.884 (5)
$M_{0d\text{(O-O)basal}}$	380 (10)		$M_{14.54d\text{(O-O)basal}}$	591 (126)

Notes: Volume (*V*), lattice parameters (K_0), and moduli (M_0) are given in Å^3, Å, and GPa, respectively. M1 is the Ca site in ank-ord and ank-ord-II, whereas it is the only cation site in ank-dis. M2 is the (Mg,Fe) site in ank-ord and ank-ord-II, whereas it is not present in ank-dis given the $R\bar{3}c$ symmetry. Results of the reference pressure for the BM fittings are 0.0001 GPa for ank-ord and ank-dis. As for ank-ord-II, reference pressure is 13.45 GPa for unit-cell parameters, and 14.54 GPa for polyhedra.

Ank-dis at ambient conditions is slightly less compressible [$K_0 = 99$ (1) GPa] than ank-ord [$K_0 = 95$ (1) GPa], and it becomes less stiff with increasing *P*, given the $K' < 4$ (Table 3; Fig. 2a). Beyond the phase transition, ank-ord-II is considerably less compressible than ank-ord.

Crystal structure evolution with *P*

The onset pressure for the phase transition from ank-ord to ank-ord-II was considered as the first point at which data could not be indexed anymore in $R\bar{3}$ symmetry, namely 13.45 GPa. However, the crystal structure refinement of ank-ord-II at this point was not satisfactory, and so only the unit-cell parameters were used for compressibility analysis.

Layers of Ca and (Mg,Fe) cations are stacked along the **c** axis in ank-ord alternated by CO_3^{2-} groups and lie in the *ab* plane (Fig. 1a), whereas they lie in the $(01\bar{1})$ plane (Fig. 1b) in ank-ord-II. The unique O position in the asymmetric unit of ank-ord, with multiplicity 6, is replaced by six non-equivalent positions in ank-ord-II (from O1 to O6, as listed in the Online Materials[1] CIF), due to the decrease in symmetry from $R\bar{3}$ (ank-ord) to $P\bar{1}$ (ank-ord-II). Furthermore, Ca, Mg, and Fe in ank-ord-II are not at special positions in the triclinic structure. Carbon, which is at a special position (0, 0, z_C) in ank-ord (Fig. 3c), occurs at two non-equivalent general sites in ank-ord-II (C1 and C2 in Fig. 3d).

Cation polyhedra were constructed for a coordination sphere with radius up to 2.9 Å, for which Ca and Mg/Fe in both ank-ord and ank-dis are 6-coordinated, as is usually observed in rhombohedral carbonates (Dem'yanov and Polestshuk 2023), with six equivalent cation-oxygen bond distances. In ank-ord-II, Ca and (Mg,Fe) polyhedra are no longer regular and cation-oxygen bond distances differ from each other. The complete list of each non-equivalent cation-oxygen distance in ank-ord-II is given in Online Materials[1] Table S2 together with the polyhedral

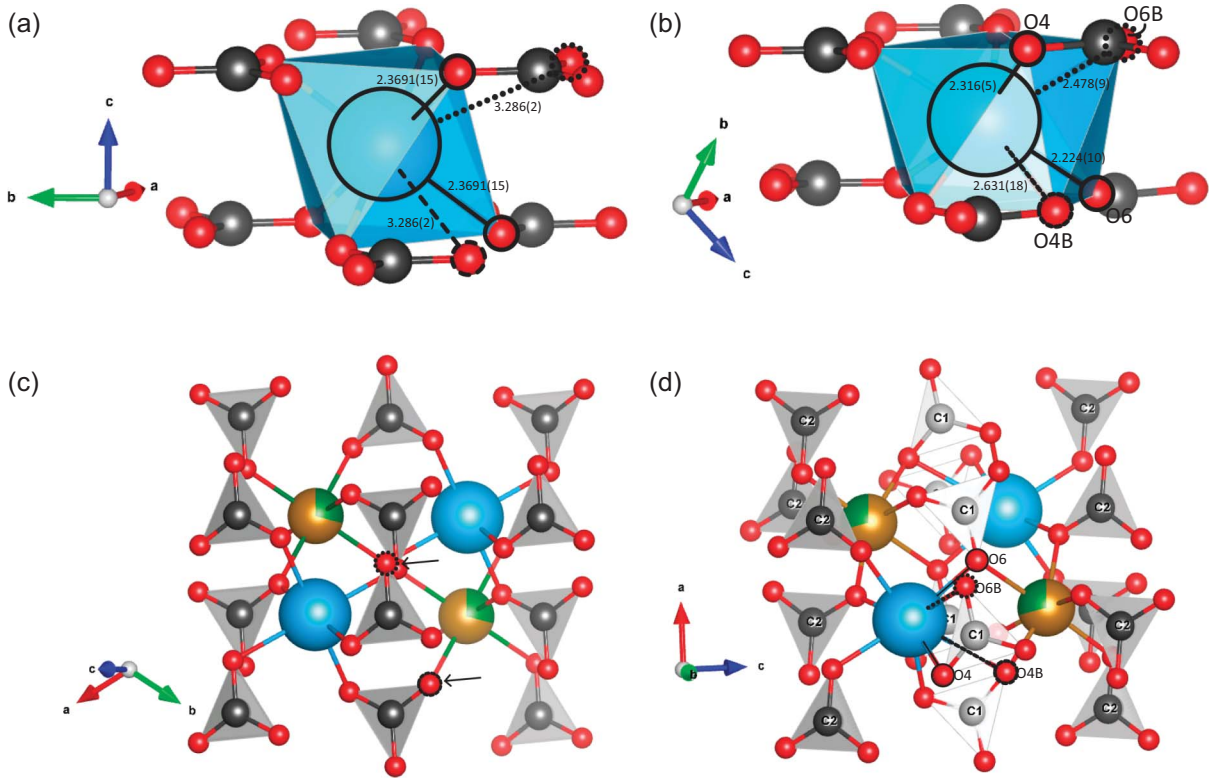

Figure 3. Crystal structure of (**a**, **c**) ank-ord at 0.47 GPa and (**b**, **d**) ank-ord-II at 21.97 GPa. Different portions of the crystal structures and selected atoms are shown to facilitate the visual comparison between ank-ord and ank-ord-II. In ank-ord-II, the increase in coordination number of the Ca site is shown in the $(01\bar{1})$ crystallographic plane in (**b**), and the C1 (light gray) and C2 (dark gray) location is given in (**d**). Arrows in (**a**) and (**c**) indicate the two O atoms, namely O6B as dashed circle and O4B as filled line circle that do not fall within the Ca polyhedra in CaO_6. For colors of the other elements, refer to Figure 1. (Color online.)

geometries for the three analyzed samples and shown in Online Materials[1] Figure S2. For ank-ord-II, the coordination number of Ca increases from 6 to 8 (Figs. 3a and 3b), including two long Ca-O bonds (Ca-O4B and Ca-O6B in Fig. 3b). The two additional O atoms bonded to Ca are related by symmetry to O4 and O6 and are here denoted O4B and O6B, as shown in Figure 3. Ca-O4B and Ca-O6B are oriented on the same side (Figs. 3b and 3d), bonded to O atoms of the group $C1O_3^{-2}$ and accommodated by a slight rotation of the $C1O_3^{-2}$ group in the *ac* plane of ~2°, anticlockwise in Figure 3d, with respect to $C2O_3^{-2}$. Data shown in Online Materials[1] Table S2 for crystal structures after decompression show that Ca polyhedron in ank-ord recovers the 6-coordination and that polyhedral dimensions for both ank-ord and ank-dis are essentially the same, within errors, as the starting structures at room *P*. Thus, the polyhedral geometry also allows to confirm the complete reversibility of the phase transition from ank-ord to ank-ord-II.

Compressibility analysis of the cation polyhedra performed by applying the second-order BM EoSs is given in Table 3. In the ordered crystal structures, the Ca polyhedron is much softer than $(Mg,Fe)O_6$ and this behavior is more evident in ank-ord-II, where the different compressibility between the two cation polyhedra is very large, being $K_{14.54}(CaO_8) = 81(10)$ GPa and $K_{14.54}[(Mg,Fe)O_6] = 186(52)$ GPa. The only cation site in ank-dis has a compressibility [$K_0 = 79.7(7)$ GPa, Table 3] much more similar to that of the CaO_6 octahedron [$K_0 = 81(1)$ GPa, Table 3] than that of the $(Mg,Fe)O_6$ [$K_0 = 91(2)$ GPa, Table 3] in ank-ord.

The distortion of the Ca and (Mg,Fe) polyhedra is analyzed using selected polyhedral volume distortion parameters (Makovicky and Balić-Žunić 1998; Zucchini et al. 2022) as shown in Figure 4 and listed in Online Materials[1] Table S2. The low-pressure polymorph of ordered ankerite regularizes as *P* increases with a steeper decrease of CaO_6 polyhedral volume distortion than that of $(Mg,Fe)O_6$ (Fig. 4). After the phase transition, the distortion strongly increases in both cation polyhedra (Fig. 4) with the highest distortions in CaO_8, which tends to decrease as *P* increases. On the contrary, MgO_6 distortion continuously increases with *P* after the phase transition. The polyhedra distortion for ank-dis follows a different behavior as it decreases as *P* increases, reaching full regularization at ~19 GPa (Fig. 4). However, no phase transition was observed up to 25 GPa.

The increase in coordination number of the Ca site in ank-ord-II is clearly seen in the evolution of the Ca-O distance above 3.2 Å in ank-ord ($Ca\text{-}O_{out}$). At the transition, this bond becomes two non-equivalent bonds, Ca-O4B and Ca-O6B, both shorter than 2.9 Å (Fig. 5a). As a consequence, the average <Ca-O> distance as well as the compressibility of the Ca polyhedron in ank-ord-II are higher than that of the other crystal structures (Table 3; Fig. 5b). In Figure 5b the average <Mg,Fe-O> in ank-ord-II is

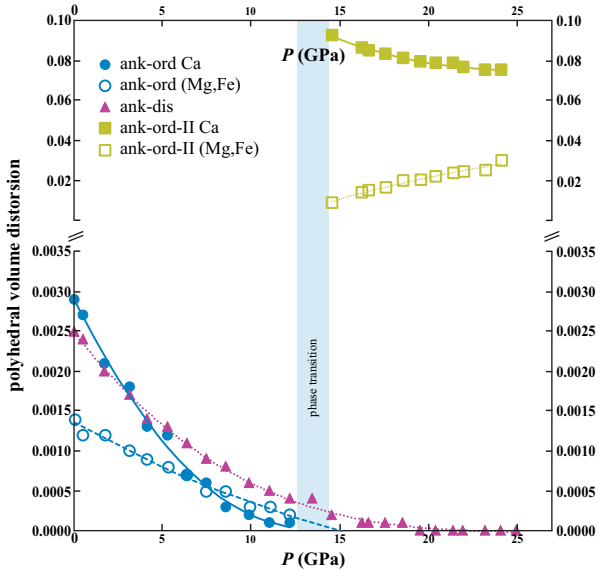

Figure 4. Polyhedral distortion for ank-ord, ank-dis, and ank-ord-II. Lines are polynomial trendlines used as guides for reader's eye. (Color online.)

shown to be almost incompressible as P increases, in agreement with the high stiffening of MgO_6 in the HP polymorph of ankerite.

In their study of dolomite, Zucchini et al. (2014) recognized "basal" and "lateral" O···O distances, hereafter referred as O···O_{basal} and O···$O_{lateral}$. These distances are affected differently by the increase in P. A graphical explanation of the meaning of O···O_{basal} and O···$O_{lateral}$ is given in Figure 1; O···O_{basal} distances are those that lie on the ab plane in ank-ord and ank-dis, whereas for ank-ord-II (triclinic) they lie on $\{01\bar{1}\}$; O···$O_{lateral}$ distances are vertically located with respect to O···O_{basal} and link adjacent CO_3 layers. In Online Materials[1] Table S2, the O···O distances of the cation polyhedra are listed for the three crystal structures. In all three crystal structures, the average O···$O_{lateral}$ distance has a higher compressibility than O···O_{basal} (Table 3), this difference being consistent with the higher compressibility of the c lattice parameter (and b in ank-ord-II) with respect to a. Moreover, among the full set of O···O_{basal} distances in $(Mg,Fe)O_6$ polyhedra, two particular edges, O5-O3 and O1-O3 (Online Materials[1] Table S2) lengthen with increasing P, a behavior that underlies the observed very low compressibility of $(Mg,Fe)O_6$ polyhedra in ank-ord-II.

Discussion

Behavior of ankerite at HP and comparison with dolomite

The phase transition from ank-ord to ank-ord-II occurs between 12.15 and 13.45 GPa. Upon phase transition, a discontinuity in the unit-cell volume is observed. Extrapolating the unit-cell volume of the high-pressure phase at lower pressure (Fig. 2a) using the EoS parameters reported in Table 3, we obtain a transition pressure of about 11.04 GPa, i.e., slightly lower than the pressure at which we still observe ank-ord to be stable. This suggests that the displacive phase transition from ank-ord to ank-ord-II is slightly first-order. Ank-dis is stable up to the maximum pressure reached in this study (~25 GPa), demonstrating that cation disorder inhibits the transition.

The bulk modulus and first pressure derivative obtained in this study for ank-ord are in agreement, within experimental errors, with recent data reported by Chuliá-Jordán et al. (2021) for an ankerite sample of similar composition and state of order (Fig. 2a), for which $K_0 = 89(4)$ GPa and $K' = 5.3(8)$. The larger K' obtained in the previous study might be due to the different method used for data collection, that is, X-ray powder diffraction in Chuliá-Jordán et al. (2021) compared with SC-XRD in the present work.

The ordered and disordered ankerite samples show different compressibility behaviors. Ank-dis is less compressible than ank-ord and has a K' significantly <4, suggesting that the change in stiffness with pressure is less pronounced than that observed for ank-ord. CaO_6 is more compressible than $(Mg,Fe)O_6$ in ank-ord, with the latter playing the major role in the ank-ord bulk compressibility (Table 3). The compressibility of the cation site in ank-dis (which is randomly occupied by Ca, Mg, and Fe) [$K_0 = 79.7(7)$ GPa, Table 3] is similar to that of CaO_6 in the ank-ord structure [$K_0 = 81(1)$ GPa, Table 3], which may explain

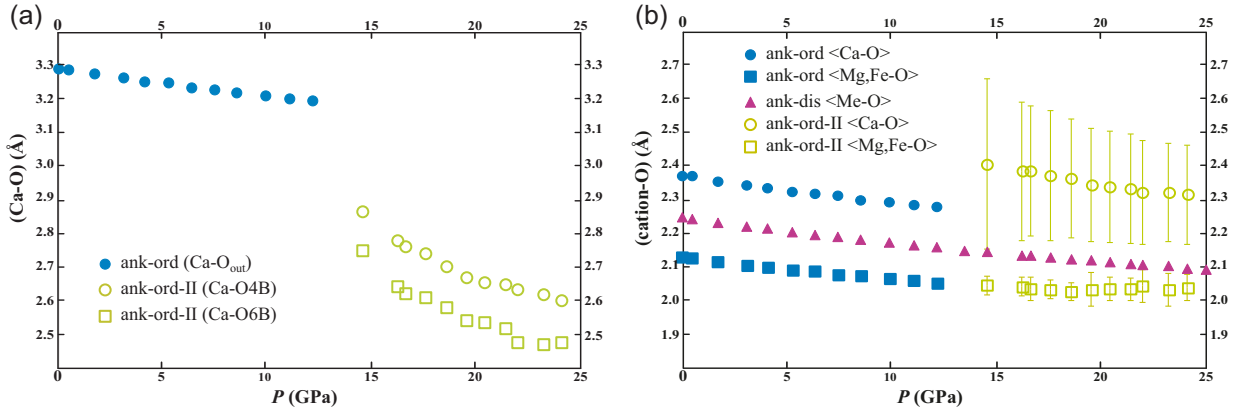

Figure 5. (**a**) Variation of Ca-O4B and Ca-O6B with P for ank-ord-II, shown together with data for the bond distance between Ca and the nearest oxygen outside the coordination polyhedron (Ca-O_{out}) in ank-ord; (**b**) Evolution with pressure of the cation to anion distances. For ank-dis, the cation to anion distance is given as <Me-O>, where Me is the cationic site with mixed occupancy (Ca,Mg,Fe). (Color online.)

why the bulk compressibility of ank-dis decreases with respect to ank-ord as P increases ($K' < 4$). Ank-ord-II is considerably less compressible than ank-ord and it stiffens at a higher rate ($K' > 4$). This behavior can be attributed to the very low compressibility of the (Mg,Fe)O_6. The total volume contraction of CaO_8 between 14.54 and 24.10 GPa is ~8%, whereas for (Mg,Fe)O_6 it is ~3%.

Ank-ord regularizes as P increases with a steeper decrease of polyhedral volume distortion of CaO_6 than that of (Mg,Fe)O_6 (Fig. 4). Beyond the phase transition, a different behavior was observed for Ca and Mg polyhedra. On the one hand, the distortions in CaO_8 in ank-ord-II is quite higher than that of the other polyhedra, and it tends to decrease with further P increase. The high distortion in Ca polyhedron in ank-ord-II is related to the increase in the Ca coordination number and the entrance in the coordination sphere of the two distant O atoms, i.e., O4B and O6B. The deformation of Ca polyhedra in ank-ord-II is also related to a strong increase in its eccentricity, that is zero in both ank-ord and ank-dis (Online Materials[1] Table S2), and reflects in the formation of CaO_8 chains that run along the a axis with Ca polyhedra sharing two lateral edges, namely O6B-O6 and O4B-O4 (Fig. 6). The (Mg,Fe)O_6 polyhedron in ank-ord-II also increases its eccentricity, as well as its distortion, with respect to ank-ord and, contrary to CaO_8, its distortion keeps increasing with P (Fig. 5; Online Materials[1] Table S2).

The HP behavior of ankerite is similar to that of dolomite. In particular, the transition pressure for ank-ord is lower than ~17 GPa observed for ordered dolomite (Merlini et al. 2012; Zucchini et al. 2017; Zhao et al. 2020), indicating that Fe has a significant effect on the transition pressure of carbonates in the system $FeCO_3$-$MgCO_3$-$CaCO_3$. The behavior of disordered ankerite resembles that of disordered dolomite, which was experimentally found to be stable at least up to 17 GPa (Zucchini et al. 2014) and predicted to be stable by ab initio calculations up to 26 GPa (Zucchini et al. 2017). The similarity between ankerite and dolomite is also shown in the evolution of octahedral distortion, which is similar in ordered ankerite and dolomite, and that approaches zero at the transition pressure, followed by a marked increase after the phase transition in both structures.

Fully disordered ankerite and dolomite show an increase in their bulk compressibility as P increases with respect to the ordered forms, having $K' = 2.7(1)$ for the former (Table 3) and $K' = 3.0(2)$ for the latter (Merlini et al. 2016); whereas, in partially disordered $R\bar{3}$ dolomite [$s = 0.26(6)$, Zucchini et al. 2014], no differences were observed with respect to the fully ordered sample with the same chemical composition. Therefore, only at fully disordered conditions, where the space group changes from $R\bar{3}$ to $R\bar{3}c$, both dolomite and ankerite appear to accommodate more easily changes in pressure.

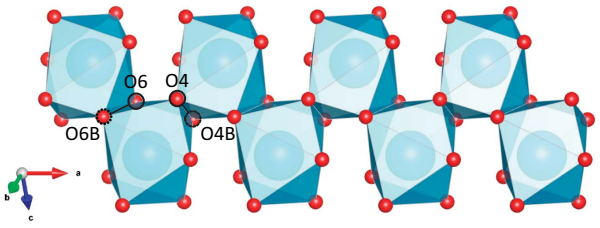

Figure 6. Slab of the supercell built from the unit cell of ank-ord-II at 14.54 GPa that shows the edge sharing on the most eccentric part of the Ca polyhedra. The shared edges are indicated with dotted (O4B-O4) and dashed (O6B-O6) lines. For colors, refer to Figure 1. (Color online.)

Strain analysis and expansion of the *a* axis

To locate the most compressible directions in the triclinic ank-ord-II structure and to investigate the geometrical reasons for the negative compressibility of the **a** axis, the magnitude and the orientation of the principal unit-strain coefficients were calculated by means of the STRAIN software as implemented in EosFit7c (Angel et al. 2014). For comparison, the strain magnitude in ank-ord and ank-dis was also calculated. Finite Lagrangian strain components were calculated with respect to the unit-cell axes measured at room pressure for ank-ord and ank-dis and with respect to the unit-cell axes at 13.45 GPa for ank-ord-II. Note that, for symmetry reasons, the principal strain components of ank-ord and ank-dis are only two, namely ε_1 and ε_3, and they have the same directions as the **a** and **c** axes, respectively. The strain calculation for the triclinic structure of ank-ord-II was performed using Cartesian axes oriented with X//a* and Y//b (Brown et al. 2006). The obtained principal strain components and their orientation with respect to the triclinic unit-cell axes at each pressure are given in Online Materials[1] Tables S3 and S4 and shown in Figure 7. The three strain vectors (ε_1, ε_2, ε_3) in ank-ord-II are also depicted in Figure 8 to better visualize their direction with respect to the atomic structure.

A strong anisotropic behavior of the magnitude of the principal strains is observed in both the rhombohedral and the triclinic ankerite structures. In particular, in ank-ord, at the transition pressure, $\varepsilon_1:\varepsilon_3 = 1.00(1):3.29(2)$, whereas the difference is less pronounced in ank-dis, where $\varepsilon_1:\varepsilon_3 = 1.00(1):2.54(1)$, at the same pressure (12.15 GPa), becoming $\varepsilon_1:\varepsilon_3 = 1.00(1):2.74(1)$, at the highest pressure point (24.10 GPa). This anisotropic behavior is in agreement with data for dolomite reported in Zucchini et al. (2014) where the **c** axis was shown to be ~3 times more compressible than the **a** axis. In ank-ord-II, $\varepsilon_1:\varepsilon_2:\varepsilon_3 = 1.0(1):–1.26(1):–0.878(7)$ at the first point after the transition (14.54 GPa) and it becomes $\varepsilon_1:\varepsilon_2:\varepsilon_3 = 1.00(1):–2.34(2):–1.560(5)$ at the highest

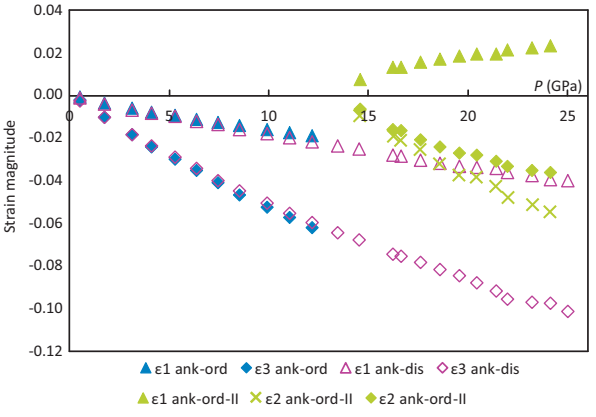

Figure 7. Magnitude of the calculated strains for the three crystal structures. (Color online.)

pressure point measured. It is clear that the anisotropic behavior of the three strain components in ank-ord-II is particularly due to the negative value of ε_1, meaning that the crystal structure expands along this direction, whereas it compresses along ε_2 and ε_3 with a higher magnitude in the former with respect to the latter.

As listed in Online Materials[1] Table S4, the negative ε_1 direction is 30° away from the **a** axis, and as such it explains the expansion of the *a* lattice parameter as *P* increases. Given the proximity of the direction of ε_1 to the [2$\bar{1}$0] lattice vector (Online Materials[1] Table S4) it is also very likely that the increase of the γ angle as *P* increases influences the sign of ε_1. Moreover, in Figure 8a it can be noticed that ε1 is parallel to several structural features that expand, instead of decreasing, as *P* increases (Online Materials[1] Table S2; Fig. 8b): O2-O4 and O6-O5 in CaO_8, which are the only oxygen-oxygen edges that expands in this polyhedron and O1-O3 in $(Mg,Fe)O_6$. As for ε_2 and ε_3, results showed that: (1) ε_2 is the softest direction and runs on the same direction of some $O\text{-}O_{lateral}$ in both CaO_8 and $(Mg,Fe)O_6$ (Fig. 8b) that, as previously observed, are the softest directions in these polyhedra (Table 3) and (2) ε_3 is stiffer than ε_2 and it is close to the [111] direction that lies on the (01$\bar{1}$) plane. This means that ε_3 lies on approximately the same plane as $O\text{-}O_{basal}$ in both CaO_8 and $(Mg,Fe)O_6$ (Fig. 3b), in agreement with the calculated low compressibility of the basal edges of polyhedra.

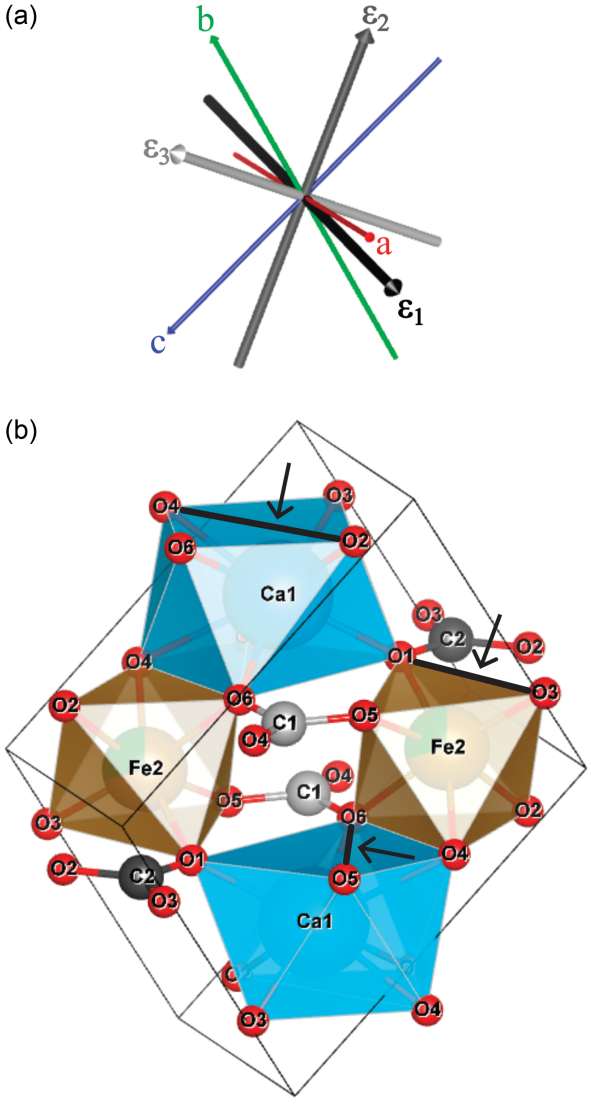

Figure 8. Directions of ε1, ε2, and ε3 with respect to *a*, *b*, and *c* orientation (**a**), crystal structure of ank-dis-II at 21.97 GPa, oriented as shown in (**a**), showing the polyhedral edges and the angle in $C1O_3$ that expand as *P* increases related to ε1 (**b**). (Color online.)

Implications

Carbonates can be important components of the lithologies involved in subducting materials from both oceanic and continental crust (e.g., Arzilli et al. 2023; Merlini et al. 2012; Poli et al. 2009). The low geothermal gradient in the subduction zones, due to the relatively cold sediments and fluids being subducted along with old and cold lithosphere, allows carbonates to come across the optimal conditions for cation disordering, that is, *T* in the range from 750 to 1200 °C (T_c for ankerite and dolomite, respectively) and pressure lower than 4 GPa. As shown in the sketch view in Figure 9, this scenario is easily achieved in warm subduction paths, such as, for example, the Mexico subduction zone as well as North Cascadia and South Chile slabs (Syracuse et al. 2010), characterized by thermal gradients in the range from

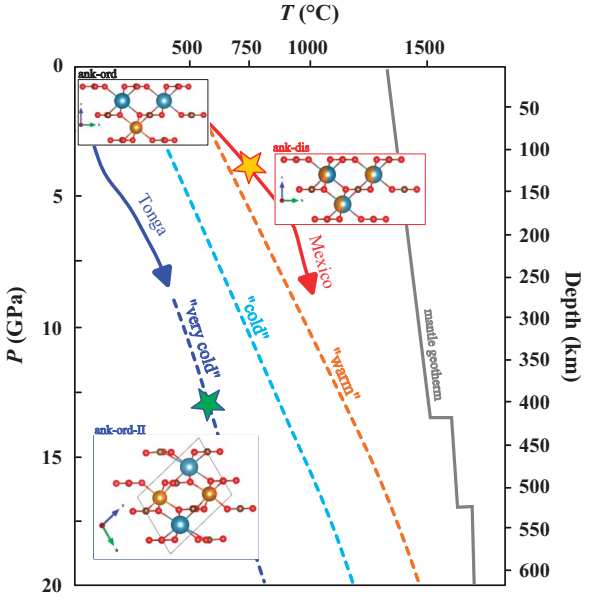

Figure 9. Paths of different subduction slabs depending on their *P-T*-depth regime: blue and red solid arrows are Tonga (coldest) and Mexico (hottest) subduction paths from Syracuse et al. (2010), respectively; dashed lines show hypothetical models from Komabayashi et al. (2004) for "very cold" (blue), "cold" (light blue), and "warm" (orange) slabs. The mantle geotherm is shown in gray. Yellow stars are the transition points from ank-ord to ank-dis shown in warm paths. The green star is the transition point from ank-ord to ank-ord-II in the very cold path. The three different ankerite structures (ank-ord, ank-ord-II, and ank-dis) are associated with the subduction regimes based on the results of the present study. Modified from Maeda et al. (2017). (Color online.)

~8 to 12 °C/km (Bang et al. 2021). In a cold regime, Figure 9 shows how very low geothermal gradients, even lower than 5 °C/km (e.g., Syracuse et al. 2010; Zheng 2019; Bang et al. 2021; van Keken and Wilson 2023), are needed for ankerite to maintain its ordered state and, thus, encounter the ankerite-I to ankerite-II phase transition. Such conditions might be found in "very cold" slabs such as Tonga (shown in Fig. 9) and Kermandec. Moreover, it is important to notice that the influence of P on T_c has not been tested so far; that is, the proposed scenarios could vary depending on how the critical temperature for disordering is influenced by pressure.

In principle, the clear differences in compressibility of ordered rhombohedral and triclinic ankerite arising from the rhombohedral → triclinic phase transition might contribute to detectable differences in the seismic signature of deeply carbonate-rich subducted material. This possibility can be explored from the data reported in this paper by calculating the bulk sound velocity $v_\Phi = (K/\rho)^{1/2}$ for each crystal structure at upper mantle pressure and room temperature. In Figure 10, we reported the v_Φ as a function of P for the here analyzed ankerite samples, together with data for other carbonate and non-carbonate minerals (Chantel et al. 2012; Zucchini et al. 2014; Zhang et al. 2019; Chariton et al. 2020; Li et al. 2023). At $P < 4$ GPa, ank-ord has the lowest values of v_Φ, whereas at $P > 4$ GPa v_Φ of ank-dis becomes the slowest one, due to the lower K' of this structure. After the phase transition, ank-ord-II initially exhibits the slowest v_Φ values that, however, rapidly increase as P increases due to its large K', becoming the fastest among the ankerite structures at $P > 18$ GPa, and approaching the behavior of both siderite and Fe-magnesite.

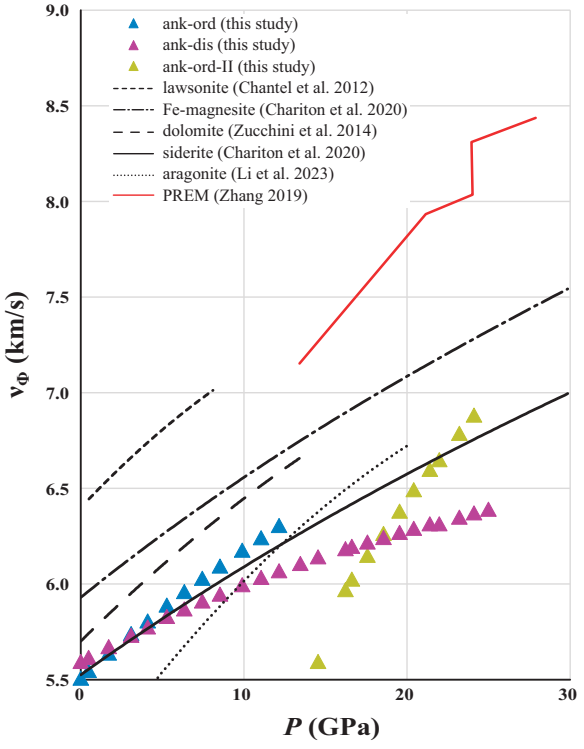

Figure 10. Bulk sound velocities as a function of pressure for the samples analyzed in the present work, as well as for different samples from literature (see the legend on the figure). The black curves are referred to v_Φ data extrapolated from literature data, given as polynomial trendlines, to make the figure easy to read. (Color online.)

These observations may help to better constrain the low-velocity layer (LVL) observed between the subducted oceanic crust and the surrounding mantle at 100–250 km depth (e.g., Chantel et al. 2012 and references therein). Several reasons for the observed low-velocity anomalies have been proposed, involving the effect of lattice preferred orientation (LPO) in minerals such as olivines (e.g., Buttles and Olson 1998; Faccenda and Capitanio 2013), chloritoid (Lee et al. 2021), talc (Mainprice et al. 2008), and lawsonite (Chantel et al. 2012; Boffa Ballaran and Angel 2003; Connolly and Kerrick 2002), that gives rise to an anisotropic behavior of seismic wave propagation along different directions in their crystal structure. Moreover, recent data from Li et al. (2023) invoked aragonite as an additional agent for the LVL occurrence, having much lower sound velocities between 4 and 10 GPa (room T) than other carbonate minerals, as well as a common pyrolytic mantle. As disordered ankerite is expected in the mantle wedge at 150–250 km depth, it might strongly impact the decrease of the sound velocities of the assemblages in subducting slabs to a depth of 250 km. Moreover, even if still unexplored, the strong anisotropic elastic behavior of ankerite and other carbonates, and that of their HP polymorphs (e.g., present paper and Zucchini et al. 2014), at HP conditions, might enhance the LPO of the subducting carbonate crystals, with respect to the subduction edge, also contributing to an anisotropic propagation of the elastic waves in those structures.

Below 300 km depth, the subducted oceanic crust does not exhibit low-velocity anomalies, likely due to the complete dehydration of lawsonite and the gradual decarbonization of the subducted oceanic crust (Li et al. 2023). Based on the bulk sound velocities here measured, at ~18 GPa the v_Φ of ank-ord-II becomes the fastest. In "very cold" regimes where ankerite might escape disordering and undergo phase transition, it might be claimed as partially contributing to the high-velocity structure of the subducted crust at these depths.

Further effort is needed to study the effect of P on T_c and the elasticity of ankerite and other Fe-bearing carbonates, which may be dependent on cation ordering, at HP and HT conditions. Several implications are expected. On the one hand, the possible subduction regimes where ankerite is either stabilized in its ordered form down to ~400 km, i.e., ~13 GPa (transition pressure), or it becomes disordered and thus stabilized, before phase transition, will be assessed. On the other hand, the analysis of the complete elastic tensor of Fe-carbonates will allow to: (1) retrieve their Vp–Vs paths; (2) analyze the sound wave propagation in the different directions of their crystal structures; and (3) give insights on the contribution of ankerite and other carbonate minerals to the sound wave anomalies registered from the Earth mantle.

Concluding Remarks

• Our HP synchrotron SC-XRD study has quantitatively constrained the effect of cation disorder on the compressibility and HP

crystal structure of ankerite. This study has shown that: (1) a rhombohedral → triclinic phase transition in ankerite at ~13 GPa only occurs in the ordered structure, and (2) the compressibilities of the two ordered structures are quite different, with the triclinic structure being much less compressible. The structure of ordered ankerite was shown to regularize as P increases up to the phase transition, which was located in the range 12.15–13.54 GPa. Above the transition P, distortion strongly increases and ank-ord-II becomes distorted with respect to ank-ord. At the phase transition, the coordination number of Ca increases from 6 to 8 and the space group changes from $R\bar{3}$ to $P\bar{1}$. Disordered ankerite also regularizes as P increases, and the cation sites are fully regular above 19 GPa. No phase transition was observed in ank-dis up to the highest P investigated (~25 GPa).

• Compressibility analysis of ank-ord and ank-dis showed that disordering has a significant influence on the EoS of ankerite, being ank-dis less compressible than ank-ord at ambient pressure but becoming more compressible as P increases ($K' < 4$). After the phase transition, ank-ord-II has a considerably low compressibility, with the $(Mg,Fe)O_6$ polyhedra almost incompressible but strongly distorted as P increases. In all three crystal structures, <Ca-O> and $<O\text{-}O>_{lateral}$ distances and, in turn, the c lattice parameter, have the highest compressibilities with respect to <Mg-O> and $<O\text{-}O>_{basal}$. The a lattice parameter always has the lowest compressibility, even expanding in ank-ord-II, together with the γ angle that increases as P increases [from 91.22(3)° at 13.45 GPa to 94.54 (2)° at 24.10 GPa]. This behavior can be attributed to the deformation of the cation layers in ank-ord-II with increasing P.

• We speculate that in "very cold" subduction regimes, where ankerite escapes the breakdown to siderite+aragonite, the onset conditions for disordering might not be achieved and ankerite takes the path of phase transition to ankerite-II.

• The calculated bulk sound velocities exhibit different variations in the three analyzed ankerite samples and disordered ankerite, likely occurring in the mantle wedge at 150–250 km depth, shows the lowest values among them, suggesting that this phase may play a role in determining the low-velocity anomalies observed in the mantle wedge. Moreover, the strong anisotropic behavior of ankerite and other carbonates, as well as that of their HP polymorphs, might enhance the LPO of the subducting carbonate crystals concerning the subduction edge, acting as a conditioning factor for the observed seismic wave anomalies. These observations are the basis for speculating that the mineral physics of ankerite might significantly contribute to the observed seismic anisotropies and large delay times in the mantle wedge. However, further effort is still needed to accurately assess the elasticity of ankerite and other carbonate minerals at contemporarily HP and HT conditions with different degrees of cation disordering.

Acknowledgments and Funding

The present work was partially funded by "DFG Core Facility for High Pressure Research" funding program in 2018, "SIMP Research Grant in Crystal-chemistry, in memory of Prof. Fiorenzo Mazzi" in 2022, and MIUR project no. PRIN2017-2017LMNLAW "Connect4Carbon." The European Synchrotron Facility is acknowledged for allocating beamtime for the experiment ES-988 (main proposer Azzurra Zucchini). We thank Tonči Balic-Žunic for kindly providing the natural ankerite sample, Ross Angel for his help with the strain analysis, and Catherine McCammon for her assistance with piston-cylinder experiments to produce the annealed sample. The comments and suggestions of Mark Welch, an anonymous reviewer, and the associate editor Simon Redfern on reviewing the manuscript are greatly acknowledged.

References Cited

Angel, R.J., Gonzalez-Platas, J., and Alvaro, M. (2014) EosFit-7c and a Fortran module (library) for equation of state calculations. Zeitschrift für Kristallographie, 229, 405–419.

Arzilli, F., Burton, M., La Spina, G., Macpherson, C.G., van Keken, P.E., and McCann, J. (2023) Decarbonation of subducting carbonate-bearing sediments and basalts of altered oceanic crust: Insights into recycling of CO_2 through volcanic arcs. Earth and Planetary Science Letters, 602, 117945, https://doi.org/10.1016/j.epsl.2022.117945.

Balić Žunić, T. and Makovicky, E. (1996) Determination of the centroid or "the best centre" of a coordination polyhedron. Acta Crystallographica Section B, 52, 78–81, https://doi.org/10.1107/S0108768195008251.

Bang, Y., Hwang, H., Kim, T., Cynn, H., Park, Y., Jung, H., Park, C., Popov, D., Prakapenka, V.B., Wang, L., and others. (2021) The stability of subducted glaucophane with the Earth's secular cooling. Nature Communications, 12, 1496, https://doi.org/10.1038/s41467-021-21746-8.

Biellmann, C. and Gillet, P. (1992) High-pressure and high-temperature behaviour of calcite, aragonite and dolomite; a Raman spectroscopic study. European Journal of Mineralogy, 4, 389–394, https://doi.org/10.1127/ejm/4/2/0389.

Binck, J., Chariton, S., Stekiel, M., Bayarjargal, L., Morgenroth, W., Milman, V., Dubrovinsky, L., and Winkler, B. (2020) High-pressure, high-temperature phase stability of iron-poor dolomite and the structures of dolomite-IIIc and dolomite-V. Physics of the Earth and Planetary Interiors, 299, 106403, https://doi.org/10.1016/j.pepi.2019.106403

Birch, F. (1952) Elasticity and constitution of Earth's interior. Journal of Geophysical Research: Solid Earth, 57, 227–286, https://doi.org/10.1029/JZ057i002p00227.

Boffa Ballaran, T. and Angel, R.J. (2003) Equation of state and high-pressure phase transitions in lawsonite. European Journal of Mineralogy, 15(2), 241–246, https://doi.org/10.1127/0935-1221/2003/0015-0241.

Brown, J.M., Abramson, E.H., and Angel, R.J. (2006) Triclinic elastic constants for low albite. Physics and Chemistry of Minerals, 33, 256–265, https://doi.org/10.1007/s00269-006-0074-1.

Buob, A., Luth, R.W., Schmidt, M.W., and Ulmer, P. (2006) Experiments on $CaCO_3$-$MgCO_3$ solid solutions at high-pressure and temperature. American Mineralogist, 91, 435–440, https://doi.org/10.2138/am.2006.1910.

Buttles, J. and Olson, P. (1998) A laboratory model of subduction zone anisotropy. Earth and Planetary Science Letters, 164, 245–262, https://doi.org/10.1016/S0012-821X(98)00211-8.

Cerantola, V., Bykova, E., Kupenko, I., Merlini, M., Ismailova, L., McCammon, C., Bykov, M., Chumakov, A.I., Petitgirard, S., Kantor, I., and others. (2017) Stability of iron-bearing carbonates in the deep Earth's interior. Nature Communications, 8, 15960, https://doi.org/10.1038/ncomms15960.

Chantel, J., Mookherjee, M., and Frost, D.J. (2012) The elasticity of lawsonite at high pressure and the origin of low velocity layers in subduction zones. Earth and Planetary Science Letters, 349, 116–125.

Chariton, S., McCammon, C., Vasiukov, D.M., Stekiel, M., Kantor, A., Cerantola, V., Kupenko, I., Fedotenko, T., Koemets, E., Hanfland, M., and others. (2020) Seismic detectability of carbonates in the deep Earth: A nuclear inelastic scattering study. American Mineralogist, 105, 325–332, https://doi.org/10.2138/am-2020-6901.

Chuliá-Jordán, R., Santamaria-Perez, D., Ruiz-Fuertes, J., Otero-de-la-Roza, A., and Popescu, C. (2021) Compressibility and phase stability of iron-rich ankerite. Minerals, 11, 607, https://doi.org/10.3390/min11060607.

Connolly, J.A.D. and Kerrick, D.M. (2002) Metamorphic controls on seismic velocity of subducted oceanic crust at 100–250 km depth. Earth and Planetary Science Letters, 204, 61–74, https://doi.org/10.1016/S0012-821X(02)00957-3.

Dem'yanov, P.I. and Polestshuk, P.M. (2023) Carbonates of alkaline earth metals: Impact of the cation size on strengths of interionic interactions and polymorphic preferences. Polyhedron, 243, 116533, https://doi.org/10.1016/j.poly.2023.116533.

Efthimiopoulos, I., Jahn, S., Kuras, A., Schade, U., and Koch-Müller, M. (2017) Combined high-pressure and high-temperature vibrational studies of dolomite: Phase diagram and evidence of a new distorted modification. Physics and Chemistry of Minerals, 44, 465–476, https://doi.org/10.1007/s00269-017-0874-5.

Faccenda, M. and Capitanio, F.A. (2013) Seismic anisotropy around subduction zones: Insights from three-dimensional modeling of upper mantle deformation and SKS splitting calculations. Geochemistry, Geophysics, Geosystems, 14, 243–262, https://doi.org/10.1002/ggge.20055.

Franzolin, E., Merlini, M., Poli, S., and Schmidt, M.W. (2012) The temperature and compositional dependence of disordering in Fe-bearing dolomites. American Mineralogist, 97, 1676–1684, https://doi.org/10.2138/am.2012.4126.

Gavryushkin, P.N., Martirosyan, N.S., Inerbaev, T.M., Popov, Z.I., Rashchenko, S.V., Likhacheva, A.Y., Lobanov, S.S., Goncharov, A.F., Prakapenka, V.B., and Litasov, H.D. (2017) Aragonite-II and $CaCO_3$-VII: New high-pressure, high-temperature polymorphs of $CaCO_3$. Crystal Growth & Design, 17, 6291–6296, https://doi.org/10.1021/acs.cgd.7b00977.

Gonzalez-Platas, J., Alvaro, M., Nestola, F., and Angel, R.J. (2016) EosFit7-GUI: A new graphical user interface for equation of state calculations, analyses and teaching. Journal of Applied Crystallography, 49, 1377–1382, https://doi.org/10.1107/S1600576716008050.

Hammersley, A.P., Svensson, S.O., Hanfland, M., Fitch, A.N., and Häusermann, D. (1996) Two-dimensional detector software: From real detector to idealized image or two-theta scan. High Pressure Research, 14, 235–248, https://doi.org/10.1080/08957959608201408.

Hammouda, T., Andrault, D., Koga, K., Katsura, T., and Martin, A.M. (2011) Ordering in double carbonates and implications for processes at subduction zones. Contributions to Mineralogy and Petrology, 161, 439–450, https://doi.org/10.1007/s00410-010-0541-z.

Harris, M.J., Dove, M.T., Swainson, I.P., and Hagen, M.E. (1998) Anomalous dynamical effects in calcite $CaCO_3$. Journal of Physics Condensed Matter, 10, L423–L429, https://doi.org/10.1088/0953-8984/10/25/002.

Hatch, D. and Merrill, L. (1981) Landau description of the calcite-$CaCO_3$ (II): Phase transition. Physical Review B: Condensed Matter, 23, 368–374, https://doi.org/10.1103/PhysRevB.23.368.

Hübschle, C.B., Sheldrick, G.M., and Dittrich, B. (2011) *ShelXle*: A Qt graphical user interface for *SHELXL*. Journal of Applied Crystallography, 44, 1281–1284, https://doi.org/10.1107/S0021889811043202.

Klotz, S., Chervin, J.C., Munsch, P., and Le Marchand, G. (2009) Hydrostatic limits of 11 pressure transmitting media. Journal of Physics D: Applied Physics, 42, 075413, https://doi.org/10.1088/0022-3727/42/7/075413.

Komabayashi, T., Omori, S., and Maruyama, S. (2004) Petrogenetic grid in the system MgO-SiO_2-H_2O up to 30 GPa, 1600 °C: Applications to hydrous peridotite subducting into the Earth's deep interior. Journal of Geophysical Research: Solid Earth, 109, B03206, https://doi.org/10.1029/2003JB002651.

Lee, J., Mookherjee, M., Kim, T., Jung, H., and Klemd, R. (2021) Seismic anisotropy in subduction zones: Evaluating the role of chloritoid. Frontiers in Earth Science, 9, 644958, https://doi.org/10.3389/feart.2021.644958.

Li, X., Zhang, Z., Lin, J.-F., Ni, H., Prakapenka, V.B., and Mao, Z. (2018) New high pressure phase of $CaCO_3$ at the topmost lower mantle: Implication for the Deep Mantle Carbon Transportation. Geophysical Research Letters, 45, 1355–1360, https://doi.org/10.1002/2017GL076536.

Li, L., Yu, Y., Mao, Z., Zhang, W., Lu, J., and Li, X. (2023) Low-velocity structure of subducted oceanic crust in the upper mantle: Insights from high pressure and temperature elasticity measurements of aragonite. Journal of Geophysical Research: Solid Earth 128, e2023JB027838.

Litasov, K., Shatskiy, A., Podborodnikov, I., and Arefiev, A. (2020) Phase diagrams of carbonate materials at high pressures, with implications for melting and carbon cycling in the deep Earth. In C.E. Manning, J.-F. Lin, and W.L. Mao, Eds., Carbon in Earth's Interior, p. 137–165. Wiley.

Liu, X. and Zhao, D. (2017) P-wave anisotropy, mantle wedge flow and olivine fabrics beneath Japan. Geophysical Journal International, 210, 1410–1431, https://doi.org/10.1093/gji/ggx247.

Luth, R.W. (2001) Experimental determination of the reaction aragonite + magnesite = dolomite at 5–9 GPa. Contributions to Mineralogy and Petrology, 141, 222–232, https://doi.org/10.1007/s004100100238.

Maeda, F., Ohtani, E., Kamada, S., Sakamaki, T., Hirao, N., and Ohishi, Y. (2017) Diamond formation in the deep lower mantle: A high-pressure reaction of $MgCO_3$ and SiO_2. Scientific Reports, 7, 40602, https://doi.org/10.1038/srep40602.

Mainprice, D., Le Page, Y., Rodgers, J., and Jouanna, P. (2008) Ab initio elastic properties of talc from 0 to 12 GPa: Interpretation of seismic velocities at mantle pressures and prediction of auxetic behaviour at low pressure. Earth and Planetary Science Letters, 274, 327–338, https://doi.org/10.1016/j.epsl.2008.07.047.

Makovicky, E. and Balić-Žunić, T. (1998) New measure of distortion for coordination polyhedra. Acta Crystallographica Section B, 54, 766–773, https://doi.org/10.1107/S0108768198003905.

Mao, H.K., Xu, J., and Bell, P.M. (1986) Calibration of the ruby pressure gauge to 800 kbar under quasi-hydrostatic conditions. Journal of Geophysical Research: Solid Earth, 91, 4673–4676, https://doi.org/10.1029/JB091iB05p04673.

Merlini, M., Crichton, W.A., Hanfland, M., Gemmi, M., Müller, H., Kupenko, I., and Dubrovinsky, L. (2012) Structures of dolomite at ultrahigh pressure and their influence on the deep carbon cycle. Proceedings of the National Academy of Sciences of the United States of America, 109, 13509–13514, https://doi.org/10.1073/pnas.1201336109.

Merlini, M., Sapelli, F., Fumagalli, P., Gatta, G.D., Lotti, P., Tumiati, S., Abdellatief, M., Lausi, A., Plaisier, J., Hanfland, M., and others. (2016) High-temperature and high-pressure behavior of carbonates in the ternary diagram $CaCO_3$-$MgCO_3$-$FeCO_3$. American Mineralogist, 101, 1423–1430, https://doi.org/10.2138/am-2016-5458.

Merlini, M., Cerantola, V., Gatta, G.D., Gemmi, M., Hanfland, M., Kupenko, I., Lotti, P., Müller, H., and Zhang, L. (2017) Dolomite-IV: Candidate structure for a carbonate in the Earth's lower mantle. American Mineralogist, 102, 1763–1766, https://doi.org/10.2138/am-2017-6161.

Merril, L. and Basset, W.A. (1975) The structure of $CaCO_3$(II): A high-pressure metastable phase of calcium carbonate. Acta Crystallographica, Section B, 31, 343–349, https://doi.org/10.1107/S0567740875002774.

Oganov, A.R., Ono, S., Ma, Y., Glass, C.W., and Garcia, A. (2008) Novel high-pressure structures of $MgCO_3$, $CaCO_3$ and CO_2 and their role in Earth's lower mantle. Earth and Planetary Science Letters, 273, 38–47, https://doi.org/10.1016/j.epsl.2008.06.005.

Pippinger, T., Miletich, R., Merlini, M., Lotti, P., Schouwink, P., Yagi, T., Crichton, W.A., and Hanfland, M. (2015) Puzzling calcite-III dimorphism: Crystallography, high-pressure behavior, and pathway of single-crystal transitions. Physics and Chemistry of Minerals, 42, 29–43, https://doi.org/10.1007/s00269-014-0696-7.

Poli, S., Franzolin, E., Fumagalli, P., and Crottini, A. (2009) The transport of carbon and hydrogen in subducted oceanic crust: An experimental study to 5 GPa. Earth and Planetary Science Letters, 278, 350–360, https://doi.org/10.1016/j.epsl.2008.12.022.

Reeder, R.J. and Wenk, H.R. (1983) Structure refinements of some thermally disordered dolomites. American Mineralogist, 68, 769–777.

Ross, N.L. and Reeder, R.J. (1992) High-pressure structural study of dolomite and ankerite. American Mineralogist, 77, 412–421.

Syracuse, E.M., van Keken, P.E., and Abers, G.A. (2010) The global range of subduction zone thermal models. Physics of the Earth and Planetary Interiors, 183, 73–90, https://doi.org/10.1016/j.pepi.2010.02.004.

van Keken, P.E. and Wilson, C.R. (2023) An introductory review of the thermal structure of subduction zones: III—Comparison between models and observations. Progress in Earth and Planetary Science, 10, 57, https://doi.org/10.1186/s40645-023-00589-5.

Vennari, C.E. and Williams, Q. (2018) A novel carbon bonding environment in deep mantle high-pressure dolomite. American Mineralogist, 103, 171–174, https://doi.org/10.2138/am-2018-6270.

Zhang, J., Martinez, I., Guyot, F., and Reeder, R.J. (1998) Effects of Mg–Fe^{2+} substitution in calcite-structure carbonates: Thermoelastic properties. American Mineralogist, 83, 280–287, https://doi.org/10.2138/am-1998-3-411.

Zhang, Y., Zhang, Y., Liu, Y., and Liu, X. (2019) A metastable Fo-III wedge in cold slabs subducted to the lower part of the mantle transition zone: A hypothesis based on first-principles simulations. Minerals, 9, 186, https://doi.org/10.3390/min9030186.

Zhao, C., Xu, L., Gui, W., and Liu, J. (2020) Phase stability and vibrational properties of iron-bearing carbonates at high pressure. Minerals, 10, 1142, https://doi.org/10.3390/min10121142.

Zhao, X., Zheng, Z., Chen, J., Gao, Y., Sun, J., Hou, X., Xiong, M., and Mei, S. (2022) High *P-T* calcite-aragonite phase transitions under hydrous and anhydrous conditions. Frontiers in Earth Science, 10, 907967, https://doi.org/10.3389/feart.2022.907967.

Zheng, Y.-F. (2019) Subduction zone geochemistry. Geoscience Frontiers, 10, 1223–1254, https://doi.org/10.1016/j.gsf.2019.02.003.

Zhu, Y. and Ogasawara, Y. (2002) Carbon recycled into deep Earth: Evidence from dolomite dissociation in subduction-zone rocks. Geology, 30, 947–950, https://doi.org/10.1130/0091-7613(2002)030<0947:CRIDEE>2.0.CO;2.

Zucchini, A., Comodi, P., Katerinopoulou, A., Balic-Zunic, T., McCammon, C., and Frondini, F. (2012a) Order-disorder-reorder process in thermally treated dolomite samples: A combined powder and single crystal X-ray diffraction study. Physics and Chemistry of Minerals, 39, 319–328, https://doi.org/10.1007/s00269-012-0489-9.

Zucchini, A., Prencipe, M., Comodi, P., and Frondini, F. (2012b) Ab initio study of cation disorder in dolomite. Calphad, 38, 177–184, https://doi.org/10.1016/j.calphad.2012.07.001.

Zucchini, A., Comodi, P., Nazzareni, S., and Hanfland, M. (2014) The effect of cation ordering and temperature on the high-pressure behaviour of dolomite. Physics and Chemistry of Minerals, 41, 783–793, https://doi.org/10.1007/s00269-014-0691-z.

Zucchini, A., Prencipe, M., Belmonte, D., and Comodi, P. (2017) Ab initio study of the dolomite to dolomite-II high-pressure phase transition. European Journal of Mineralogy, 29, 227–238, https://doi.org/10.1127/ejm/2017/0029-2608.

Zucchini, A., Balić-Žunić, T., Collings, I.E. , Hanfland, M., and Comodi, P. (2022) High-pressure single-crystal synchrotron X-ray diffraction study of lillianite. American Mineralogist, 107, 1752–1759, https://doi.org/10.2138/am-2021-7765.

Manuscript received June 11, 2024
Manuscript accepted October 11, 2024
Accepted manuscript online October 15, 2024
Manuscript Handled by Simon A.T. Redfern

Endnotes:

[1]Deposit item AM-25-69495. Online Materials are free to all readers. Go online, via the table of contents or article view, and find the tab or link for supplemental materials. The CIF has been peer-reviewed by our Technical Editors.